Peer reviewed version of the manuscript accepted for publication in Nature Materials (2018)

doi:10.1038/s41563-017-0014-0

Cell geometry dependent changes in plasma membrane order direct stem cell signalling and fate

Thomas C. von Erlach[1,2,3], Sergio Bertazzo[1,4], Michele A. Wozniak[5], Christine-Maria Horejs[1,2,3], Stephanie A. Maynard[1,2,3], Simon Attwood[2], Benjamin K. Robinson[2], Hélène Autefage[1,2,3], Charalambos Kallepitis[1,2,3], Armando Del Rio Hernandez[1], Christopher S. Chen[5,6,7], Silvia Goldoni[1, 2,3*], Molly M. Stevens[1, 2,3*]

[1] Department of Materials, Imperial College London, London, UK

[2]Department of Bioengineering, Imperial College London, London, UK

[3] Institute of Biomedical Engineering, Imperial College London, London, UK

[4]Department of Medical Physics & Biomedical Engineering, University College London, London, UK

[5] Department of Bioengineering, University of Pennsylvania, Philadelphia, USA

[6] Department of Biomedical Engineering and the Biological Design Center, Boston University, Boston, MA, USA

[7] The Wyss Institute for Biologically Inspired Engineering, Harvard University, Boston, MA, USA.

[*]Correspondence should be addressed to S.G. (e-mail: s.goldoni22@gmail.com) and M.M.S. (e-mail: m.stevens@imperial.ac.uk)

Cell size and shape affect cellular processes such as cell survival, growth and differentiation[1-4], thus establishing cell geometry as a fundamental regulator of cell physiology. The contributions of the cytoskeleton, specifically actomyosin tension, to these effects have been described, but the exact biophysical mechanisms that translate changes in cell geometry to changes in cell behaviour remain mostly unresolved. Using a variety of innovative materials techniques, we demonstrate that the nano-structure and lipid assembly within the cell plasma membrane are regulated by cell geometry in a ligand-independent manner. These biophysical changes trigger signalling events involving the serine/threonine kinase Akt/PKB that direct cell geometry dependent mesenchymal stem cell differentiation. Our study defines a central regulatory role by plasma membrane ordered lipid raft microdomains in modulating stem cell differentiation with potential translational applications.

Proteomics and FRET imaging studies suggest that cytoskeletal proteins interact and associate with plasma membrane lipid raft microdomains[5], which are important regulators of cell signalling[6]. Using model membranes, it was proposed that the formation of actin cytoskeleton networks induces membrane phase separation and heterogeneity, indicating lipid raft formation[7]. Thus, events resulting in enhanced formation of cytoskeletal networks, such as integrin engagement with the extracellular matrix and focal adhesion formation were found to increase membrane order[8], a biophysical hallmark of lipid rafts[9,10]. We hypothesized that cell architecture related changes in cytoskeletal networks modulate lipid rafts independently of soluble extracellular cues. As a result, the biophysical state of the cytoskeleton directly regulates the activity of cell signalling proteins associated with plasma membrane micro-domains. Although this has been shown in differentiated cell types, the relationship between rafts and cytoskeleton in mesenchymal stem cell function and fate is largely unknown. We cultured human mesenchymal stem cells (hMSC) on surfaces micropatterned with fibronectin

islands of triangular, square and circular geometries with identical surface area (1350 μm^2). Cells adhered to fibronectin and displayed distinct morphologies and cytoskeletal arrangement dictated by island geometries (Fig. 1a and b). Fluorescence intensity heatmaps of F-actin and myosin IIa highlighted differences in cell contractility amongst the three geometries (Fig. 1c). Analysis of the compliance of living cells by atomic force microscopy (AFM) revealed differences in shape-dependent stiffness between triangular and circular, and square and circular cells. Higher stiffness measured in triangular and square cells correlated with cell contractility (Fig. 1d). The AFM data reveal a link between cell shape and elasticity, independently of adhesion area. To observe 3D structural arrangements of the plasma membrane we developed a method to serially section cells *in situ* using focused-ion-beam coupled to imaging (FIB) (Fig.2a). 3D reconstructions of plasma membranes brought to light remarkably different topographies across cell geometries down to the nano-scale (Fig. 2b). This observation correlated with a significantly increased number of membrane invaginations in the size range of 50-100 nm, resembling caveolae, a subset of lipid rafts, in triangular compared to circular cells (Fig. 2c and d, non-treated). These data point to a connection between cell contractility and caveolae formation. Interestingly, it was previously reported that white blood cells and neurons lack caveolae despite having planar shaped lipid rafts[11]. This suggests that caveolae are a product of surface area demand and supports the notion that cells with lower cytoskeletal contractility assemble less caveolae. Thus micropatterning cells in different shapes but with the same adhesion area can decouple area and cytoskeletal contractility. Next, we analysed the number of caveolae in triangular, square and circular hMSC in the presence of Cytochalasin D, a mycotoxin that interferes with actin polymerisation. The treatment abolished cell shape-dependent differences in caveolae abundance (Fig. 2d, CytoD). Furthermore, treatment with Y27632, a ROCK (Rho-associated kinase) inhibitor that blocks myosin IIa light chain phosphorylation and consequently actomyosin contraction, had a similar effect (Fig. 2d).

As caveolae are cholesterol-rich structures, we tested methyl-β-cyclodextrin (MβCD), a cholesterol sequestering agent that disrupts the integrity of lipid rafts[12]. Treating hMSC with MβCD lowered the number of caveolae across cell shapes compared to non-treated cells and erased geometry-dependent differences (Fig. 2d; Supplementary Figure 1). Interestingly, treatment with MβCD did not impair cell spreading on fibronectin islands (Supplementary Figure 2). However, F-actin staining revealed less actin bundling and focal organization in square and triangular cells supporting the interdependence between actin cytoskeleton and lipid rafts. This interdependence has been shown in neurons where cholesterol depletion results in aberrant axonal growth and guidance[13].

We further investigated the relationship between geometrical cues and lipid rafts with total internal reflection fluorescence (TIRF) microscopy. We used FITC-conjugated cholera toxin B subunit (CTB), a GM1 gangliosides binder, and fluorescent filipin III. CTB binds specifically to lipid rafts[14], and filipin III binds cholesterol[15]. We detected higher FITC-CTB signal on the plasma membrane of triangular and square hMSC compared to circular cells (2 and 1.5 fold, respectively). The intensity of fluorescent filipin III was around 20% and 10% higher in triangular and square cells, respectively, compared to circular cells (Fig. 3a and b). The chemical heterogeneity of the plasma membrane across cell geometries correlates with the structural heterogeneity observed by FIB while the underlying biophysical mechanism and structure-function relationship are yet to be understood. Plasma membrane invaginations detected by FIB are likely caveolae based on their size and sensitivity to MβCD treatment. Because caveolae, a subtype of lipid rafts[16], are caveolin-1 positive structures, we measured caveolin-1 expression on the plasma membrane of patterned hMSC. TIRF imaging revealed around 20% more caveolin-1 expressed on the plasma membrane of triangular and square cells compared to circular cells (Fig. 3a and b) in line with the quantification of caveolae-like invaginations observed by FIB (Figure 2a-d). Average distance of cells from substrate was

comparable across shapes reducing the likelihood of differences detected by TIRF being artefactual (Supplementary Figure 3). These data indicate that cell geometry regulates the abundance of lipid rafts and caveolae. In fact, CD71, a transferrin receptor associated to non-raft membrane domains, was equally expressed on the membrane of triangular and circular cells (Fig. 3c and d). To further probe the link between cytoskeletal contractility and caveolae, we imaged CTB and caveolin-1 in the presence or absence of Y27637. Disrupting the RhoA pathway abolished cell shape-dependent differences in caveolae and lipid raft abundance (Fig. 3e and f) indicating that cytoskeletal contractility can regulate plasma membrane biophysics in an extracellular signalling-independent fashion. As expected, sequestering cholesterol with MβCD also erased cell shape-dependent modulation of lipid rafts. It appears that MβCD treatment causes redistribution of Cav-1 from the periphery into internal regions within the substrate-facing plasma membrane in circular hMSC suggesting cells are subjected to cytoskeletal rearrangement upon MβCD treatment (Supplementary Figure 4). Furthermore, the effect of cell shape on plasma membrane order was investigated by analysing giant plasma membrane vesicles (GPMVs) isolated from triangular, square and circular micropatterns using C-laurdan as reported elsewhere[17]. GPMVs from triangular cells displayed the highest membrane order (Fig. 3g and h) further suggesting that lipid rafts are more abundant in these cells. As a control, we analysed GPMVs from hMSC grown in a tissue culture flask with or without MβCD (Supplementary Figure 5).

Considering the cell signalling and endocytosis function of lipid rafts and caveolae[16], we investigated whether the observed cell geometry-dependent changes could trigger downstream signalling driving cell behaviour. It was recently reported that activity of the serine/threonine kinase Akt is regulated by its association with lipid rafts[18]. Lipid rafts facilitate recruitment to the inner leaflet of the plasma membrane and subsequent activation of Akt and its activator PDK1[19,20]. Furthermore, MβCD-mediated cholesterol depletion abolishes Akt signalling in

keratinocytes[21]. Activated by growth factors, cytokines and ligand-independent stimuli, Akt and PDK-1 are recruited to the plasma membrane resulting in the phosphorylation of Akt at T308 initiating a signal transduction cascade[22]. We measured Akt phosphorylation at the T308 site via In-Cell Western (ICW) (Fig. 4a). In line with the differential lipid raft assembly in cells displaying high cytoskeletal contractility, we found significantly higher Akt T308 phosphorylation in triangular and square cells compared to circular cells (Fig. 4f, control). Since Akt recruitment to the plasma membrane is important for its activation, we quantified Akt abundance by TIRF microscopy (Fig. 4b). We found more Akt protein on the surface of triangular and square cells compared to circular cells (Fig. 4c). To explore Akt association to lipid rafts, we analysed the correlation of Akt and CTB signals in TIRF microscopy using Pearson's coefficient. Due to the resolution limit of TIRF microscopy, the co-localization is limited to plasma membrane micro-domains. We found increased co-localisation of CTB and Akt as well as Akt and PDK1 as compared to CAV-1-Akt, cSRC-Akt, CD71-CAV-1 and CD71-CTB, supporting the existence of an interaction between Akt and PDK1 in lipid rafts (Fig. 4d). To corroborate the ICW data and validate signal specificity, we ran a western blot for pan Akt and phospho-Akt T308 using the same antibodies used in ICW (Fig. 4e). Western blots showed a decrease in Akt T308 phosphorylation in circular compared to triangular cells (non-cropped blots in Supplementary Figure 6).

We further analysed the connection between cytoskeletal contractility, lipid rafts and Akt T308 phosphorylation using chemical inhibitors. Disrupting lipid rafts by MβCD or filipin III[21,23] treatment reduced Akt T308 phosphorylation in high contractility geometries abolishing shape-dependent differences (Fig. 4f). We observed a similar effect when treating with Y27632 and CytoD (Fig. 4f). The Akt allosteric inhibitor MK2206[24] also erased shape-driven Akt T308 phosphorylation (Supplementary Figure 7). Importantly, MK2206 blocks the PH domain of Akt which is required for lipid raft association. Taken together, these data demonstrate the

existence of a previously unexplored mechanism of cell geometry-dependent Akt activation mediated by cell contractility and lipid raft formation.

In order to further understand the molecular mechanism behind Akt activation by cell shape changes, we investigated the role of the Akt upstream activator phosphatidylinositol-3 kinase (PI3K). PI3K mediates conversion of membrane phosphatidylinositol 4,5-bisphosphate (PI(4,5)P2) to phosphatidylinositol 3,4,5-trisphosphate (PI(3,4,5)P3), which recruits both Akt and its activator PDK-1 to the plasma membrane by direct interaction[25]. We overexpressed a plasma membrane-targeted, constitutively active PI3K in hMSC. As expected, engineered cells display a higher level of Akt phosphorylation compared to control cells (Supplementary Figure 8). Interestingly, hMSC with increased PI3K activity did not display significant differences in shape-dependent Akt phosphorylation compared to control cells indicating that the observed mechanism is independent of the amount of PIP3 on the plasma membrane (Fig. 4g). On the contrary, inhibition of PI3K activity by LY294002, an inhibitor of the P110 catalytic subunit, abolished shape-dependent Akt T308 phosphorylation, indicating that PIP3 is required (Fig. 4f, LY; non-normalized data are shown in Supplementary Figure 9). Additional protein kinases can be involved in this mechanism as LY294002 retains non-selective activity.

Lastly, we investigated the regulation of stem cell differentiation. Micropatterned hMSCs cultured in mixed adipogenic and osteogenic differentiation medium with low and high cytoskeletal contractility, differentiated preferentially into adipocytes and osteoblasts, respectively (Fig. 5a-c), as previously published[2,3,26]. Differentiation was assessed in binary images with colour deconvolution of 7-day cultures stained with OilRedO and for alkaline phosphatase activity (Supplementary Figure 10). Inhibition of cell contractility by Y27632 and CytoD led to the abolishment of cell shape differences since adipogenic differentiation increased by several fold in cell geometries with higher contractility (Fig. 5d). Remarkably, inhibiting lipid rafts with MβCD erased differences in lineage commitment dictated by cell

shape and treating with filipin III resulted in an increase in adipogenesis in triangular and square cells (Fig. 5d). These data bring to light the existence of a previously unknown mechanism that links lipid rafts formation to hMSC differentiation. Importantly, treatment with MK2206 shifted overall differentiation towards adipogenesis without significant cell geometry-dependent differences (Fig. 5d). These data define Akt as a major player in cell geometry-dependent osteogenesis. We propose that high cell contractility favours lipid raft formation and/or stability, triggering Akt recruitment to the plasma membrane, pathway activation and osteogenic differentiation. In line with data presented in Figure 4g, increased PI3K activity did not change cell geometry dependent differentiation (Fig. 5e). Interestingly, FIB cross-sections of whole hMSC showed characteristic lipid vacuoles (Fig. 5f). Circular hMSC carried a higher number of these structures further supporting their preferential adipogenic phenotype (Fig. 5g). This phenotype is somewhat dependent on cytoskeletal contractility and the presence of lipid rafts as treatment with CytoD and MβCD reduced the shape-dependent differences (Fig. 5g).

To conclude, by applying innovative materials and imaging techniques, we investigated the cell-substrate interface and studied plasma membrane morphology at the nano-scale level. We discovered a mechanism by which cell geometry regulates cell signalling via modulation of plasma membrane order. Changes in plasma membrane order due to geometric cues affect stem cell fate through a newly identified signalling mechanism involving Akt. Our data suggest a central role for lipid rafts in regulating cell behaviour and we propose that this mechanism allows cells to rapidly respond to changes in tissue mechanics and prepare for the integration of complex signals. Our findings expand the knowledge around tissue homeostasis mechanisms and have broad implications for regenerative medicine and tissue engineering applications[27,28].

References

1. Chen, C. S., Mrksich, M., Huang, S., Whitesides, G. M., & Ingber, D. E. Geometric Control of Cell Life and Death. *Science* **276**, 1425–1428 (1997).
2. Kilian, K. a, Bugarija, B., Lahn, B. T. & Mrksich, M. Geometric cues for directing the differentiation of mesenchymal stem cells. *Proceedings of the National Academy of Sciences of the United States of America* **107**, 4872–7 (2010).
3. McBeath, R., Pirone, D. M., Nelson, C. M., Bhadriraju, K. & Chen, C. S. Cell shape, cytoskeletal tension, and RhoA regulate stem cell lineage commitment. *Developmental Cell* **6**, 483–495 (2004).
4. Aragona, M., Panciera, T., Manfrin, A., Giulitti, S., Michielin, F., Elvassore, N., Dupont, S., et al. A mechanical checkpoint controls multicellular growth through YAP/TAZ regulation by actin-processing factors. *Cell* **154**, 1047–59 (2013).
5. Head, B. P., Patel, H. H., & Insel, P. A. Interaction of membrane/lipid rafts with the cytoskeleton: impact on signaling and function: membrane/lipid rafts, mediators of cytoskeletal arrangement and cell signaling. *Biochimica et Biophysica Acta*, **1838**(2), 532–45 (2014).
6. Simons, K. & Toomre, D. Lipid rafts and signal transduction. *Nature reviews. Molecular Cell Biology* **1**, 31–9 (2000).
7. Liu, A. P. & Fletcher, D. A. Actin polymerization serves as a membrane domain switch in model lipid bilayers. *Biophysical Journal* **91**, 4064–70 (2006).
8. Gaus, K., Le Lay, S., Balasubramanian, N. & Schwartz, M. Integrin-mediated adhesion regulates membrane order. *The Journal of Cell Biology* **174**, 725–34 (2006).
9. Head, B. P., Patel, H. H., Roth, D. M., Murray, F., Swaney, J. S., Niesman, I. R., Farquhar, M. G., Insel, P. A. Microtubules and Actin Microfilaments Regulate Lipid

Raft / Caveolae Localization of Adenylyl Cyclase Signaling Components. *Journal of Biological Chemistry*, **281**(36), 26391–26399 (2006).

10. Lingwood, D. & Simons, K. Lipid rafts as a membrane-organizing principle. *Science* **327**, 46–50 (2010).

11. Head, B. P., & Insel, P. A. Do caveolins regulate cells by actions outside of caveolae? *Trends in Cell Biology*, **17**(2), 51–57 (2007).

12. Palazzo, A. F., Eng, C. H., Schlaepfer, D. D., Marcantonio, E. E., & Gundersen, G. G. Localized stabilization of microtubules by integrin- and FAK-facilitated Rho signaling. *Science*, **303**(5659), 836–9 (2004).

13. Kamiguchi, H. The region-specific activities of lipid rafts during axon growth and guidance. *Journal of Neurochemistry*, **98**(2), 330–335 (2006).

14. Blank, N., Schiller, M., Krienke, S., Wabnitz, G., Ho, A. D., & Lorenz, H.M. Cholera toxin binds to lipid rafts but has a limited specificity for ganglioside GM1. *Immunology and Cell Biology* **85**, 378–82 (2007).

15. Wüstner, D. Fluorescent sterols as tools in membrane biophysics and cell biology. *Chemistry and Physics of Lipids* **146**, 1–25 (2007).

16. Parton, R. G., & Simons, K. The multiple faces of caveolae. *Nature reviews. Molecular cell biology* **8**, 185–94 (2007).

17. Sezgin, E., Kaiser, H.-J., Baumgart, T., Schwille, P., Simons, K., & Levental, I. Elucidating membrane structure and protein behavior using giant plasma membrane vesicles. *Nature Protocols*, ***7*(6)**, 1042–51 (2012).

18. Gao, X. & Zhang, J. Spatiotemporal Analysis of Differential Akt Regulation in Plasma Membrane Microdomains. *Molecular Biology of the Cell* **19**, 4366–4373 (2008).

19. Lasserre, R., Guo, X.-J., Conchonaud, F., Hamon, Y., Hawchar, O., Bernard, A.-M., Soudja, S. M., et al. Raft nanodomains contribute to Akt/PKB plasma membrane recruitment and activation. *Nature Chemical Biology* **4**, 538–47 (2008).

20. Gao, X., Lowry, P. R., Zhou, X., Depry, C., Wei, Z., Wong, G. W., & Zhang, J. PI3K/Akt signaling requires spatial compartmentalization in plasma membrane microdomains. *Proceedings of the National Academy of Sciences of the United States of America* ***108***(35), 14509–14 (2011).

21. Calay, D., Vind-Kezunovic, D., Frankart, A., Lambert, S., Poumay, Y., & Gniadecki, R. Inhibition of Akt signaling by exclusion from lipid rafts in normal and transformed epidermal keratinocytes. *The Journal of Investigative Dermatology*, **130**(4), 1136–45 (2010).

22. Manning, B. D. & Cantley, L. C. AKT/PKB signaling: navigating downstream. *Cell* **129**, 1261–74 (2007).

23. Schnitzer, J. E., Oh, P., Pinney, E., & Allard, J. (1994). Filipin-sensitive caveolae-mediated transport in endothelium: Reduced transcytosis, scavenger endocytosis, and capillary permeability of select macromolecules. *Journal of Cell Biology*, **127**(5), 1217–1232 (1994).

24. Hirai, H., Sootome, H., Nakatsuru, Y., Miyama, K., Taguchi, S., Tsujioka, K., et al. MK-2206, an allosteric Akt inhibitor, enhances antitumor efficacy by standard chemotherapeutic agents or molecular targeted drugs in vitro and in vivo. *Molecular Cancer Therapeutics*, **9**(7), 1956–67 (2010).

25. Vanhaesebroeck, B., Stephens, L., & Hawkins, P. PI3K signalling: the path to discovery and understanding. *Nature reviews. Molecular cell biology* **13**, 195–203 (2012).

26. Müller, P., Langenbach, A., Kaminski, A., & Rychly, J. Modulating the Actin Cytoskeleton Affects Mechanically Induced Signal Transduction and Differentiation in Mesenchymal Stem Cells. *PLoS ONE*, **8**(7), 1–8 (2013).

27. Stevens, M. M. & George, J. H. Exploring and engineering the cell surface interface. *Science* **310**, 1135–8 (2005).

28. Place, E. S., Evans, N. D. & Stevens, M. M. Complexity in biomaterials for tissue engineering. *Nature Materials* **8**, 457–70 (2009).

29. Tan, J. L., Liu, W., Nelson, C. M., Raghavan, S. & Chen, C. S. Simple approach to micropattern cells on common culture substrates by tuning substrate wettability. *Tissue Engineering* **10**, 865–72 (2004).

30. Harris A. R., Charras G. T. Experimental validation of atomic force microscopy-based cell elasticity measurements. *Nanotechnology* **22**, 1-10 (2011).

Acknowledgements

We thank Hans Markus Textor and Fabian Anderegg (ETH Zurich) for providing silicon masters for micro-contact printing as well as Stephen Rothery for training and guidance regarding TIRF microscopy (FILM facility at Imperial College London). T.v.E. was supported by an EPSRC DTA Ph.D. award. S.B. was supported by the Rosetrees Trust and the Stoneygate Trust and the Junior Research Fellowship scheme at Imperial College London. M.M.S. gratefully acknowledges ERC starting grant "Naturale" for funding (206807), Wellcome Trust Senior Investigator Award (098411/Z/12/Z) and the Rosetrees Trust.

Author Contributions

T.E. designed experiments, developed the substrates and conducted experiments, analysed and interpreted the data and wrote the manuscript. S.B. designed and carried out ion and electron

microscopy experiments and analysed the data. M.W. conducted viral transfection experiments and revised the manuscript. C.K. performed 3D plasma membrane reconstruction and analysis. B.R and S.A. conducted AFM measurements. C.H. carried out western blots. C.C. revised the manuscript and consulted in experimental design. A.D.R.H. revised the manuscript and supervised S.A. H.A. helped with hMSC cultivation and differentiation experiments and revised the manuscript. S.M. helped with cell micropattern preparations and revised the manuscript. S.G. supervised the project, helped in experimental design, data analysis and interpretation and co-wrote the manuscript. M.M.S. supervised the project, co-wrote the manuscript and helped in experimental design and data interpretation.

Competing Financial Interest

The authors declare no competing financial interests.

Data Availability

Raw data is available upon request from rdm-enquiries@imperial.ac.uk.

Methods

Generation of micropatterned substrates. Stamps were made by replica casting polydimethylsiloxane (PDMS, Sylgard 184; Dow Corning, Midland, MI, USA) against a silicon master made by photolithography (gift from Markus Textor). PDMS pre-polymer was poured over the silicon master and cured at 60 °C overnight. The elastomeric stamp bearing the negative pattern of the master was peeled off and stored dry in a closed well plate at room temperature. Stamps were sonicated for 30 minutes in ethanol, rinsed three times with distilled water, blown dry under nitrogen, oxidized in air plasma for 1 minute (200 mtorr) (Plasma Prep 5, Gala Instruments) and used for contact printing immediately. To allow adsorption of proteins, plasma-activated stamps were immersed for 1 hour in 50 µg/mL bovine fibronectin (Sigma) in phosphate-buffered saline (PBS). Stamps were blow dried by compressed air and placed in conformal contact with the substrate (non-treated polystyrene multi-dish, Nunclon Surface) for 60 seconds before being peeled off. Subsequently, substrates were immersed in 0.4 % (w/v) Pluronic F127 (Sigma) in PBS for 2 hours, and carefully rinsed with water without allowing the surface to dry. Micropatterns for TIRF were generated by using silanized glass as a substrate for cell micropattern preparation according to a protocol published previously[29].

Culture of human mesenchymal stem cells and differentiation protocol. Human mesenchymal stem cells (hMSCs) (PromoCell) were cultured in mesenchymal stem cell growth medium (PromoCell) under standard cell culture conditions (37°C, 5 % CO_2). For experiments, cells were detached by using 0.25 % (v/v) Trypsin-EDTA solution (Invitrogen) and seeded in serum free growth medium at a density of 13000 cells/ cm^2 on the micropatterned substrate. After allowing cells to adhere for 2 hours, substrate was washed with PBS and media were replaced with serum containing media.

Antibodies and reagents. Mouse monoclonal anti-phospho-Akt (T308) (1:200), anti-phospho-Akt (Ser 473), polyclonal rabbit anti Akt (1:300), polyclonal rabbit anti myosin IIa light chain (1:400), monoclonal rabbit anti CD71, monoclonal rabbit anti Src, monoclonal rabbit anti PDK-1 as well as monoclonal mouse anti phospho myosin IIa light chain (1:100) were all purchased from Cell Signaling Technology. GAPDH was bought from Ambion. FITC conjugated Cholera Toxin B subunit (1:50) as well as filipin III from Streptomyces Filipinensis (1:10) were purchased from Sigma. Alexa Fluor®488 and Alexa Fluor®568 phalloidin (1:300) and DAPI (4',6-diamidino-2-phenylindole) were all obtained from Molecular Probes (Invitrogen). Polyclonal rabbit anti caveolin-1 (1:400) was purchased from Abcam. Secondary antibodies anti-mouse Alexa Fluor®568 (1:400) and anti-rabbit Fluor®488 (1:400) were bought from Molecular Probes. Infrared secondary antibodies, IRdye 680RD goat anti-mouse IgG and IRdye 800CW anti-rabbit (both 1:1000) were purchased from LiCor. For inhibitor studies, the following concentrations were used: 2.5 µM Y27632, 40 nM Cytochalasin D (both from Sigma), 3 µM MK-2206 (Active Biochemicals), 0.5 mM methyl-β-cyclodextrin (Santa Cruz Biotechnology), 0.5 µM filipin III and 20 µM LY294002 (both from Cayman Chemicals). Concentrations were determined based on cell morphology analysis. Y27632 and methyl-β-cyclodextrin were both solubilised in PBS, all other inhibitors were solubilised in DMSO according to manufacturer instructions.

AdPI3K transfection. hMSCs were maintained in growth media (10 % (v/v) FBS in low-glucose DMEM). hMSCs were plated at a confluency of 13000 cells/cm^2 overnight, and the next day infected with either GFP or PI3K-p110CAAX ("AdPI3K") virus for 5 hours. The following day, cells were trypsinized and 13000 cells/cm^2 were plated on Pluronic-blocked micropatterned substrates in the presence of growth media or differentiation media for Akt activity assays or differentiation assays, respectively. Differentiation medium consisted of 1:1

adipogenenic:osteogenic media and was changed every 3 days. Adipogenic media contained 3 % (v/v) FBS, 1 % (v/v) penicillin-streptomycin, 500 µM IBMX, 2 µM rosiglitazone, 1 µM dexamethasone, 17 µM pantothenate, 33 µM biotin and 1 µM insulin in DMEM/F12. Osteogenic media contained 10 % (v/v) FBS, 1 % (v/v) penicillin-streptomycin, 100 nM dexamethasone, 250 µM ascorbic acid-2-phosphate and 10 mM β-glycerophosphate.

Giant plasma membrane vesicle (GPMV) isolation and analysis. GPMVs were isolated and analysed according to a previously published protocol[17]. Briefly, hMSCs were cultured on triangular, square and circular micropatterns for 24 hours, washed with GPMV buffer (10 mM HEPES, 150 mM NaCl, 2 mM $CaCl_2$, pH 7.4) and then incubated in GPMV isolation solution (25 mM Paraformaldehyde / 2 mM Dithiothreitol in GPMV buffer) for 2 hours. Afterwards, the solution was collected and transferred into bovine serum albumin coated vials. After 30 minutes, 50 µL from the bottom of the vial was transferred into a fresh bovine serum albumin coated vial and labelled with 1 µl of 0.2 mM solution of 6-Dodecanoyl-2-Dimethylaminonaphthalene (C-laurdan) (Molecular Probes) for 30 minutes.

Microscopy data analysis. For fluorescence analysis, cells grown on micropatterns were immunostained using standard procedures. Briefly, cells were fixed with 4 % (v/v) formalin in dH_2O (Sigma) for 15 minutes at room temperature, washed with PBS, permeabilised with 0.25 % (v/v) Triton-X-100/PBS for 2 minutes, washed with PBS and then blocked with 4 % (w/v) bovine serum albumin in PBS. Primary and secondary antibodies were incubated in blocking buffer for 1 hour at room temperature. For TIRF microscopy analysis using plasma membrane lipid markers CTB and filipin III, samples were not permeabilised with Triton-X-100 to preserve the plasma membrane. Only single cells that were confined into the desired shape were selected by using the microscope in brightfield mode. An Olympus BX51 upright and an Olympus inverted microscope were used to image fluorescence and phase contrast samples.

For the histological analysis, cells were inspected by phase contrast to determine whether they expressed lineage specific markers based on what has been described previously[2]. Briefly, for patterned MSCs only single cells that adhered to the pattern were used for statistical analysis. Cells that contained lipid vacuoles stained red by OilRedO were counted as adipocyte specification. Cells that stained blue for alkaline phosphatase were counted as osteoblast committed cells. For additional quantitation we performed a colour deconvolution of all cells across a surface stained with both markers based on what was published earlier[2]. Briefly, raw RGB images acquired by phase contrast with a 20x objective were imported in ImageJ, background-subtracted and afterwards colour deconvoluted by a publicly available colour deconvolution plugin for ImageJ commonly used for separating similar histology stains (http://www.dentistry.bham.ac.uk/landinig/software/cdeconv/cdeconv.html) with colour-specific vectors adapted to the particular images. The resulting separated red and blue channels were binarised with a set threshold based on visual examination and subsequently quantified. For generating immunofluorescence heatmaps, MSCs cultured on the three different shapes were imaged on the same day using the same microscope and camera settings. Raw fluorescent images were background-subtracted in ImageJ, incorporated into a Z Hyperstack and the summarised intensity was calculated for heatmap generation. For Total Internal Reflection Fluorescence (TIRF) Microscopy, samples on glass substrate (glass bottom dish, MatTek Prod. Nb P35G-0-10-C) in PBS were imaged using a Zeiss Axiovert 200 manual inverted microscope with a 488 laser diode, a 100X/1.45W Alpha Plan Fluar objective and back illuminated EM-CCD camera (Hamamatsu C9100-13). Resulting 16 bit raw images were background-subtracted and binarised for quantification purposes using ImageJ software. For high resolution co-localisation analysis, background-subtracted TIRF microscopy images of 2 different channels were merged in one image. Then the Pearson Coefficient was analysed with ImageJ using the JACoP Plugin (http://rsb.info.nih.gov/ij/plugins/track/jacop2.html). Multiphoton

imaging of C-laurdan labelled giant plasma membrane vesicles (GPMVs) was performed with an inverted Olympus IX81 microscope with a 25X water immersion long working distance objective using a MaiTaiDeepSea Laser at 800 nm excitation and emission filtered at 410-440 nm as well as at 502-548 nm.

Western blot, In-Cell Western and immunofluorescence. For In-Cell Western, cellular proteins were quantitated *in situ* based on infrared intensity. Samples were immunolabelled with an infrared conjugated IgG secondary antibody using standard immunofluorescence protocol and imaged using an Odyssey Fc Infrared Imaging System (LiCor) in the highest resolution (21 μm). The resulting signal intensity was subsequently quantified by using the Odyssey CLx Image Studio Analysis Software. For western blots, Ad(GFP) and Ad(PI3K) cells were lysed in 25 mM HEPES, 75 mM NaCl, 1 % (v/v) NP-40, 1 mM EDTA, 1× Halt protease and phosphatase inhibitor cocktail (Thermo Scientific), and centrifuged at 14000 rpm for 10 minutes at 4 °C. Lysates from cells on hydrogels were obtained with RIPA buffer (Sigma) containing protease inhibitors (Roche) and phosphatase inhibitors (Sigma). Protein concentration was determined by Precision Red Advanced Protein Assay (Cytoskeleton, Denver, CO). 10 μg of protein were separated by denaturing SDS–PAGE, transferred to PVDF membrane, blocked with 5 % (w/v) bovine serum albumin (BSA) in 0.3 % (v/v) Tween-20 in Tris-buffered saline, immunoblotted with primary antibodies (1:1000), and detected using horseradish peroxidase–conjugated secondary antibodies (1:5000; Jackson ImmunoResearch Laboratories) and SuperSignal West Dura (Pierce). Densitometric analysis was performed using a VersaDoc imaging system and QuantityOne software (Bio-Rad Laboratories), and statistically analysed using GraphPad Prism software. Western blot was performed using infrared labelled secondary antibodies, scanned and analysed using the Odyssey imaging system and software (LiCor).

Atomic Force Microscopy (AFM) analysis. hMSCs were cultured on the three micropatterned shapes for 24 hours. Samples were analysed in the petri dish in PBS at room temperature by Atomic Force Spectroscopy. A Nanowizard I (JPK, Germany) Atomic Force Microscope (AFM) with an inverted microscope (IX-81, Olympus, Germany) was used for all measurements. We used MLCT-D levers (Bruker) with a nominal spring constant of 0.03 N/m. For analysis, cantilevers were calibrated immediately before use using the thermal noise method. Polystyrene Microspheres with a diameter of 15 µm (Life Technologies) were attached to AFM cantilever tips using a UV curable glue (Loctite 350, rs-online) as described elsewhere[30]. Force-displacement curves were analysed using a custom developed routine in Matlab (MathWorks). The contact point was identified by considering each point in the approach curve and fitting the Hertz model to the contact region and a constant value for the points thereafter. The point with the smallest error for the combined fits was identified as the contact point. The Young's modulus, E, was then determined for the contact region from this point onwards. Indentation was kept below 10% of the cell height to avoid substrate effects.

Focused Ion Beam (FIB) and Scanning Electron Microscopy (SEM) analyses. Micropatterned cells were fixed in a 4 % (v/v) formaldehyde (Sigma, BioReagent, ≥ 36.0 %) with 0.2 % (v/v) glutaraldehyde (EMS – Electron Microscopy Sciences) solution in PBS at room temperature for 15 minutes. Samples were washed three times with cacodilate buffer (EMS – Electron Microscopy Sciences) and osmicated with osmium tetroxide in 2 % (w/v) cacodilate buffer for 30 minutes. After that, samples were washed five times with deionized water and then dehydrated through a graded ethanol (Sigma, ACS reagent 99.5 %) series two times for each concentration (20, 30, 40, 50 70, 80, 90, 100, 100, 100% (v/v)) for 2 minutes in each solution. After dehydration, samples were infiltrated with Epon Resin (EMS – Electron

Microscopy Sciences) diluted in ethanol at 3:1, 2:1, and 1:1 for 1 hour each, and then overnight at 1:2. The solution was then replaced with pure resin, which was changed twice in the first 12 hours and then allowed to infiltrate again overnight. After that, the maximum amount of resin was removed and the bottom of the well plate (containing the cells) was detached and centrifuged at 5000 rpm for 5 minutes. Samples were immediately placed in an oven at 60 °C and left to cure overnight. Samples were secured to a SEM aluminium sample holder with carbon tape and silver paint applied to the area immediately surrounding the sample (to maximise conductivity), and then coated with 5 nm of chromium in a sputter coater (QuorumTechnologies model K575X). Following the coating procedure, samples were introduced into an SEM/Focused Ion Beam (Carl Zeiss - Auriga) with gallium ion beam operated at 30 kV. A region over the cells with approximately 15 x 5 x 2 µm (length x height x depth) was milled using 4 nA current. After that, the region exposed by the first milling was polished with 240 pA current and imaged by a backscattering detector with the electron bean operating at 1.5 V. To generate a 3D-surface model, individual high resolution *in situ* cross-section electron micrographs of micropattered cells were stacked using MATLAB®. From these volume datasets an iso-surface was extracted based on polygonal abstraction. The area between the substrate surface and substrate facing cell plasma membrane was calculated by using the Image J software.

Statistical Analysis. All data were analysed by one-way ANOVA followed by a Tukey and Bonferroni post hoc analysis except AFM data in Fig. 1d that was analysed by one-way ANOVA followed by a Bartlett's test for equal variances. The statistical parameters are as follows: Fig. 1d (F-value = 8.18, R square = 0.04415); Fig. 2d (F-value = 7.31 p-value triangular versus square cells = 0.027, p-value triangular versus circular cells = 0.014); Fig. 3b CAV-1 (F-value = 12.04, p-value triangular versus square cells = 0.0031, p-value triangular

versus circular cells = 9.02261 × 10–6); Fig. 3b CTB (F-value = 8.64, p-value triangular versus square cells = 0.00149, p-value triangular versus circular cells = 7.84 × 10–4); Fig. 3b filipin III (F-value = 11.33, p-value circular versus square cells = 0.032, p-value triangular versus circular cells = 1.90 × 10–5); Fig. 3e (F-value = 6.65, p-value non-treated triangular versus circular cells = 1.32 × 10–5, p-value non-treated triangular versus triangular MBCD treated cells = 3.50 × 10–4, p-value non-treated triangular versus circular MBCD treated cells = 2.07 × 10–5, p-value non-treated triangular versus triangular Y27632 treated cells = 0.00356, p-value non-treated triangular versus circular Y27632 treated cells = 0.0019); Fig. 3f (F-value = 6.14, p-value non-treated triangular versus circular cells = 2.12 × 10–5, p-value non-treated triangular versus triangular MBCD treated cells = 5.34 × 10–4, p-value non-treated triangular versus circular MBCD treated cells = 9.24 × 10–4, p-value non-treated triangular versus triangular Y27632 treated cells = 0.00143, p-value non-treated triangular versus circular Y27632 treated cells = 0.00594); Fig. 3h (F-value = 45.22, p-value triangular versus square cells = 2.22 × 10–5, p-value triangular versus circular cells = 5.42 × 10–18, p-value square versus circular cells = 3.58 × 10–9); Fig. 4c (F-value = 26.42, p-value triangular versus square cells = 0.03, p-value triangular versus circular cells = 3.09 × 10–10, p-value square versus circular cells = 1.02 × 10–4); Fig. 4d (F-value = 29.91, p-values: Akt and CAV-1 versus CTB and CD71 = 0.23854, Akt and PDK1 versus CAV and CD71 = 3.99 × 10–12, Akt and PDK1 versus CTB and CD71 = 5.33 × 10–9, Akt and PDK1 versus Akt and CAV-1 = 1.38 × 10–13, Akt and CTB versus CAV and CD71 = 2.21 × 10–9, Akt and CTB versus CTB and CD71 = 2.42 × 10–6, Akt and CTB versus Akt and CAV-1 = 6.17 × 10–11, Akt and Cd71 versus Akt and CAV-1 = 0.46, Akt and Cd71 versus Akt and PDK1 = 3.01 × 10–10, Akt and Cd71 versus Akt and CTB = 1.91 × 10–7, Akt and c-Src versus Akt and CAV-1 = 0.11, Akt and c-Src versus Akt and PDK1 = 4.95 × 10–8, Akt and c-Src versus Akt and CTB = 1.75 × 10–5); Fig. 4f (F-value = 21.86, p-value triangular versus square cells = 0.03, p-value triangular

versus circular cells = 0.0014, p-value square versus circular cells = 0.046); Fig. 4g adPI3K (F-value = 5.75, p-value triangular versus circular cells = 0.048); Fig. 4g adGFP (F-value = 16.36, p-value triangular versus circular cells = 0.004); Fig. 5b (F-value = 14.09, p-value circular versus square cells = 0.002, p-value triangular versus circular cells = 3.15× 10–4); Fig. 5e adPI3K (F-value = 14.09, p-value circular versus square cells = 4.82393 × 10–4, p-value triangular versus circular cells = 2.02886 × 10–4); Fig. 5e adGFP (F-value = 27.942, p-value circular versus square cells = 0.01094, p-value triangular versus circular cells = 0.0058); Fig. 5g (F-value = 6.13, p-value triangular versus circular cells = 0.0104).

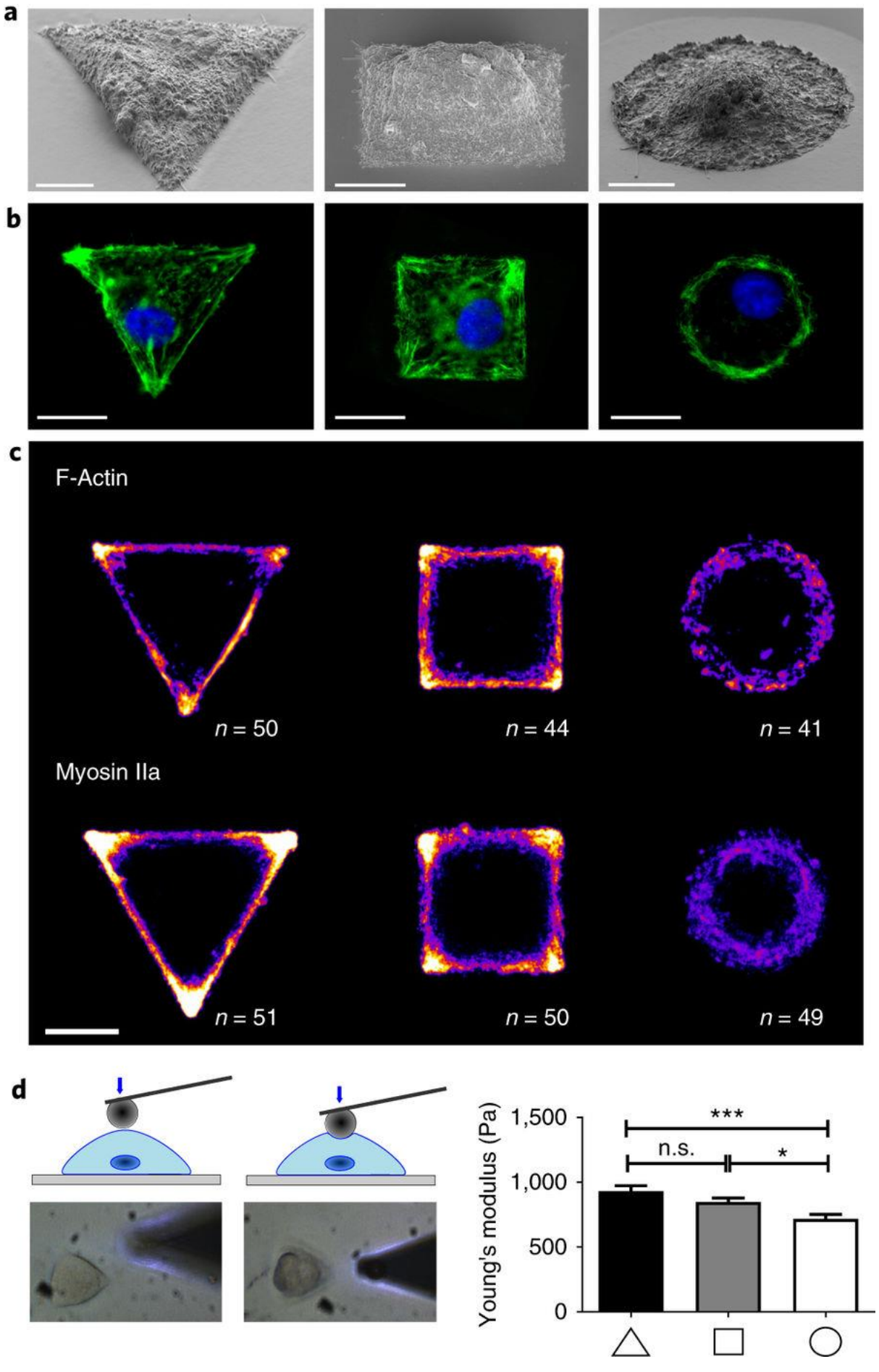
a
b
c
F-Actin
n = 50
n = 44
n = 41
Myosin IIa
n = 51
n = 50
n = 49
d
Young's modulus (Pa)
1,500
1,000
500
0
***
n.s.
*

Fig. 1 Cell geometry induces changes in cytoskeletal arrangement and cell contractility. (a) Representative SEM micrographs of micropatterned hMSC. (b) Representative immunofluorescence images of hMSC stained for F-actin (green) and Dapi (blue). (c) Immunofluorescence intensity heat maps of myosin IIa and F-actin. Higher intensity is represented by a yellow/white colour. n = number of cells used for heat map generation. Scale bar, 20 µm. (d) Live cell stiffness measurement of triangular, square and circular cells by atomic force microscopy (AFM). 30 cells per condition were analysed. * equals $p<0.05$; *** equals $p<0.001$. Error bars represent S.E.M.

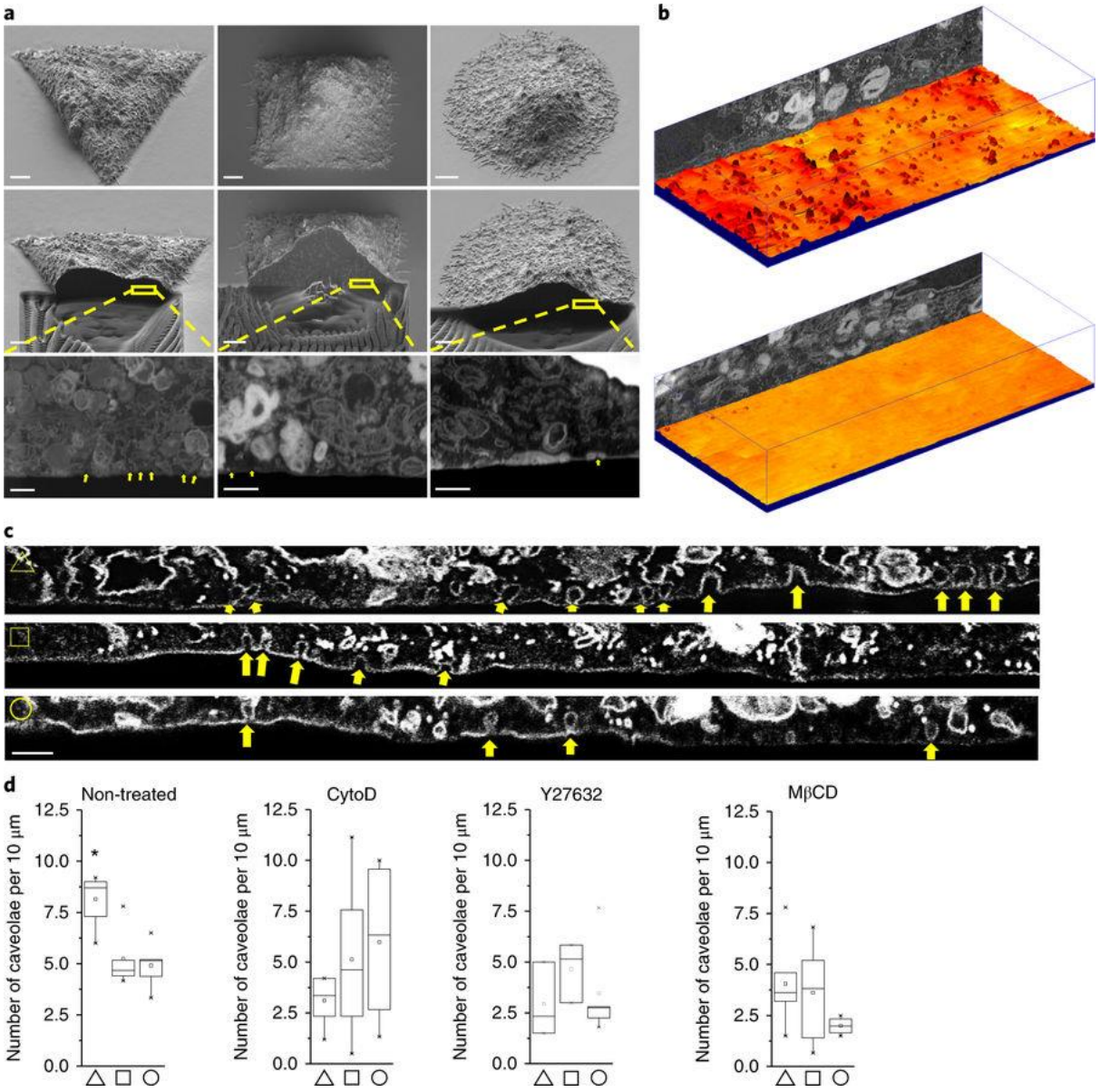

Fig. 2 Cell geometry regulates plasma membrane morphology and topography. (a) High resolution electron micrographs of cells *in situ* generated by focused ion beam microscopy. (I) SEM micrographs

of triangular, square and circular micropatterned cells; (II) micropatterned cells sectioned in the middle by focused ion beam; (III) cross-section analysed with high magnification reveals cell geometry dependent morphology of plasma membrane facing the substrate. Scale bars, 5 µm. (b) Cross-section and 3D reconstruction of plasma membrane surface illustrated as topographical heatmap based on 60 cross-sections of triangular (top) and circular (bottom) cells. (c) High magnification micrographs focusing on the plasma membrane-substrate interface reveal the presence of membrane invaginations in the range of 50-100 nm resembling caveolae (yellow arrows) Scale bar, 300 nm. (d) Number of caveolae-like structures quantified from images as in c of control hMSC and cells treated as indicated. Data are obtained from 19 to 35 cross-section images from 3 to 6 cells per shape. * equals $p<0.05$. Data are presented as box plots to show values distribution; bottom and top of box represent 25% and 75%, respectively.

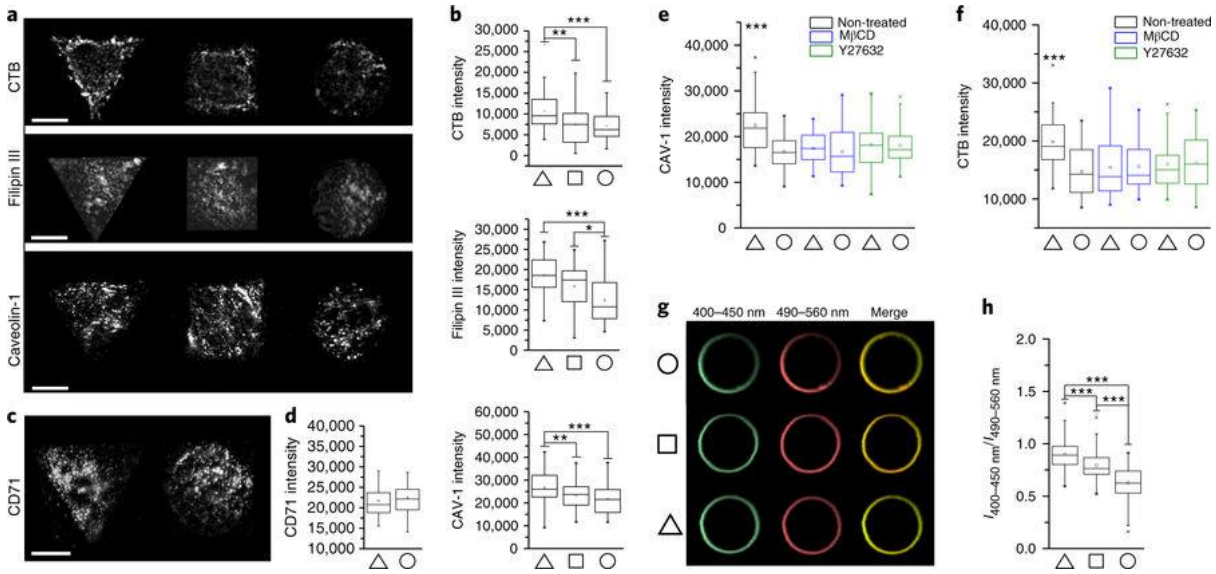

Fig. 3 Signal intensity of lipid raft markers is dependent on cell geometry. (a) Representative TIRF microscopy images of the plasma membrane-substrate interface. Cholera Toxin Subunit B (CTB) is a marker for lipid rafts and Filipin III stains for accumulation of cholesterol, a hallmark of lipid rafts. Caveolin-1 positive plasma membrane domains are a subtype of lipid rafts. Scale bars, 20 µm. (b) Quantification of TIRF images per condition and stain (n = 75–93 for CAV-1, n = 33–37 for filipin III, n = 38–53 for CTB). Box plots show complete data range, bottom and top of box represent 25% and 75%, respectively. ***, $p < 0.001$; **, $p < 0.01$; *, $p < 0.05$ (three independent experiments). c,

Representative TIRF microscopy images of triangular and circular hMSCs stained for CD71, a non-raft marker. Scale bar, 20 μm. (d) Quantification of 50 TIRF images of CD71 stained hMSC as in c (n=20-32). (e-f) Quantification of TIRF images of triangular and circular hMSC as in a, treated with either the ROCK inhibitor Y27632 or methyl-β-cyclodextrin (MβCD) (n = 35–46 for CTB and n = 29–42 for CAV-1). ***, $p < 0.001$. (g) Representative multiphoton images of C-laurdan stained giant plasma membrane vesicles (GPMVs) isolated from triangular, square or circular hMSCs with emission light filtered to select wavelengths representative of ordered (green) and disordered (red) phase. (h) Quantification of the ratio of fluorescence intensity of the ordered (green) and disordered (red) phase emission of GPMVs isolated from triangular, square or circular hMSCs (n = 51-123). Box plots show complete data range, bottom and top of box represent 25% and 75%, respectively. *** equals $p<0.001$ (3 independent experiments).

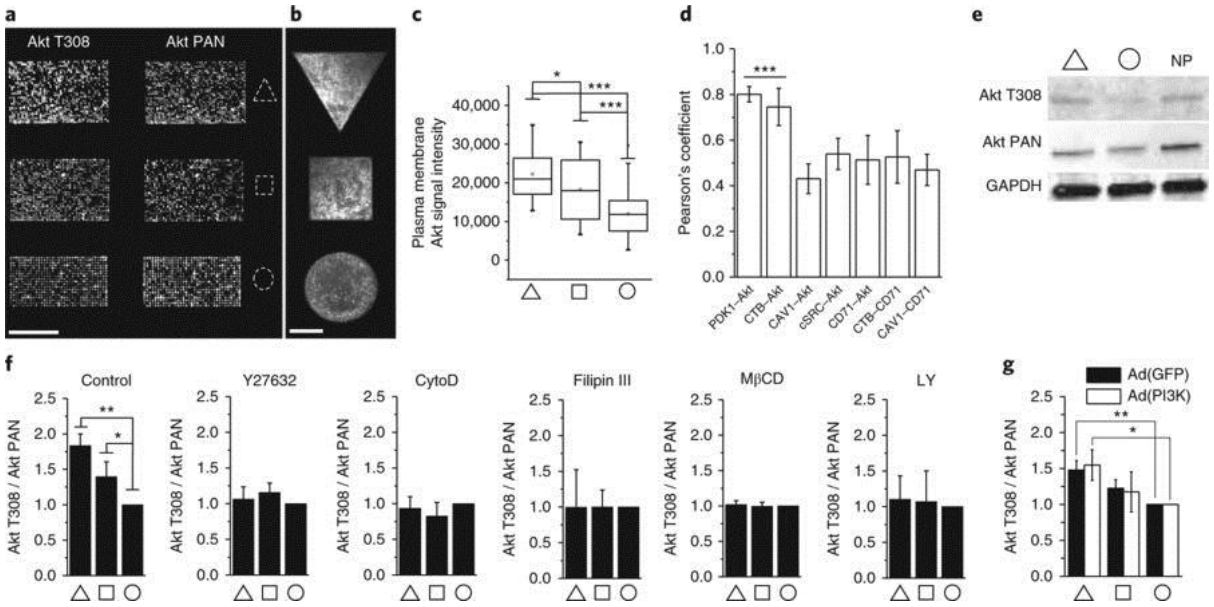

Fig. 4 Akt recruitment to the plasma membrane and activation are dependent on cell geometry. (a) Representative in-cell western images of arrays of micropatterned hMSCs (950 cells per shape). Cells were stained with phospho-Akt T308 and Quantification of TIRF images per shape (**b**), from three independent experiments. Box plots show complete data range, bottom and top of box represent 25% and 75%, respectively ($n = 34–46$). ***, $p < 0.001$; *, $p < 0.05$. (d) Co-localization analysis from TIRF images of markers indicated and Akt in triangular hMSCs quantified by the Pearson's coefficient (n = 8–

11). ***, $p < 0.001$ (e) Representative western blot of phospho-Akt T308 and pan Akt of triangular and circular as well as non-patterned (NP) hMSCs. GAPDH was used as loading control. Note that antibodies used in the western blot are the same as those used in the in-cell western assay. (f) Quantification of data from in-cell western images (a), of cells treated as indicated. CytoD, cytochalasin D; methyl-β-cyclodextrin (MβCD); LY, LY294002. Values are means ± standard deviation (s.d.). *, $p < 0.05$; **, $p < 0.01$ (three independent experiments in duplicate). (g) Quantification of phospho-Akt T308 and pan Akt by in-cell western images of hMSCs stably transfected to carry enhanced PI3K activity compared with GFP transfected control cells. Values are means ± standard deviation (s.d.). *, $p < 0.05$; **, $p < 0.01$ (three independent experiments in duplicate).

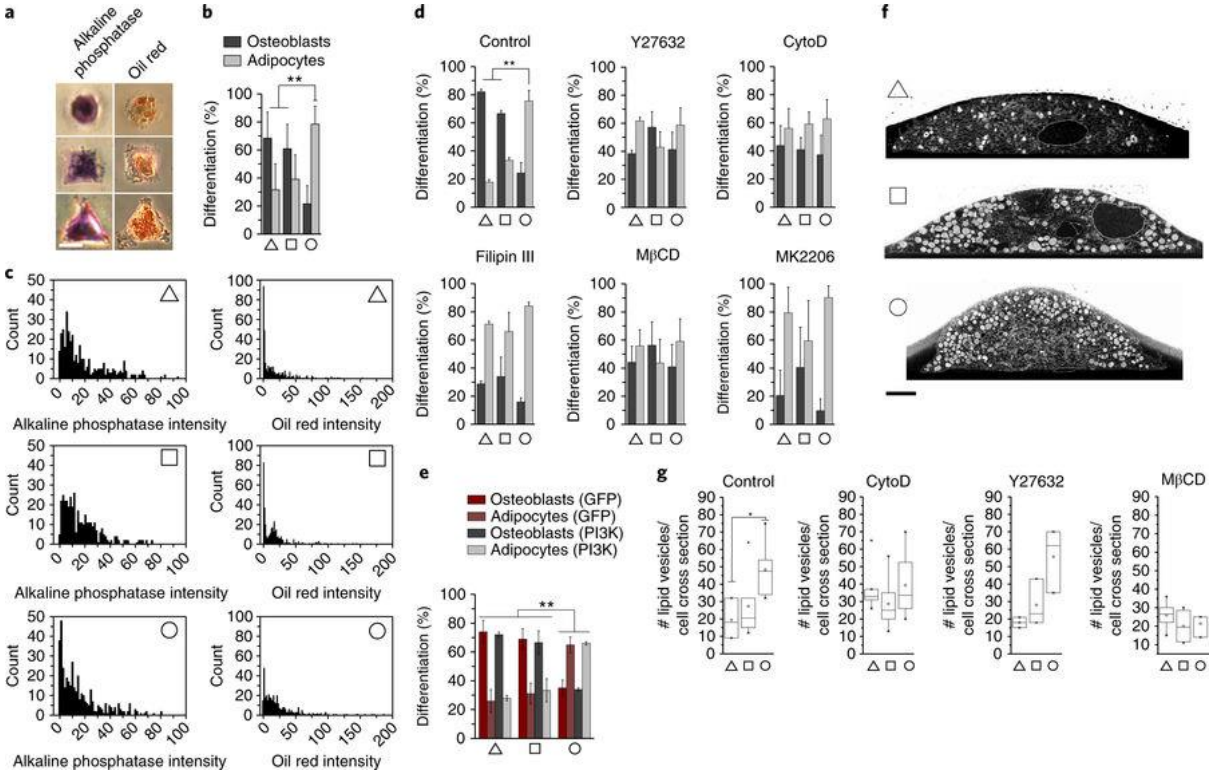

Fig. 5 Lipid rafts and Akt signalling mediate cell geometry dependent hMSC differentiation. (a) Representative images of hMSCs differentiated into either fat (OilRedO) or bone cells (alkaline phosphatase activity). Scale bar, 20 μm. (b) Quantification of differentiation of micropatterned hMSCs into either adipocytes or osteoblasts, following 7 days in the presence of a 1:1 mix of adipogenic and osteogenic differentiation medium. Compiled from cells from 7 independent experiments performed in duplicate (n = 364–392). Values are means ± s.d. **, $p < 0.01$. (c) Frequency histograms of OilRedO

and alkaline phosphatase activity corresponding to data shown in b. (d) Quantification of adipogenic and osteogenic fate (a) of micropatterned hMSCs treated as indicated. (e) Quantification of adipogenic and osteogenic fate of hMSCs transfected with constitutively active PI3K. Values are means ± s.d. **, $p < 0.01$. 100 cells per condition (three independent experiments in duplicate). (f) Representative images of whole-cell cross-sections of triangular, square and circular hMSCs reveal the presence of characteristic lipid vacuoles (white round structures). Note the high density of lipid vacuoles in circular hMSCs, supporting evidence that low cell-contractility geometries favour adipogenesis. Cells are cultured in basal medium. Scale bar, 4 μm. (g) Quantification of lipid vacuoles from whole-cell cross-sections (f) of control hMSCs and cells treated as indicated. Data are obtained from 5 to 10 cells per shape. Data are presented as box plots to show values distribution; bottom and top of box represent 25% and 75%, respectively. *, $p < 0.05$.

Cell geometry dependent changes in plasma membrane order direct stem cell signalling and fate

Thomas C. von Erlach[1,2,3], Sergio Bertazzo[1,4], Michele A. Wozniak[5], Christine-Maria Horejs[1,2,3], Stephanie A. Maynard[1,2,3], Simon Attwood[2], Benjamin K. Robinson[2], Hélène Autefage[1,2,3], Charalambos Kallepitis[1,2,3], Armando Del Rio Hernandez[1], Christopher S. Chen[5,6,7], Silvia Goldoni[1, 2,3*], Molly M. Stevens[1, 2,3*]

Supplementary Figures

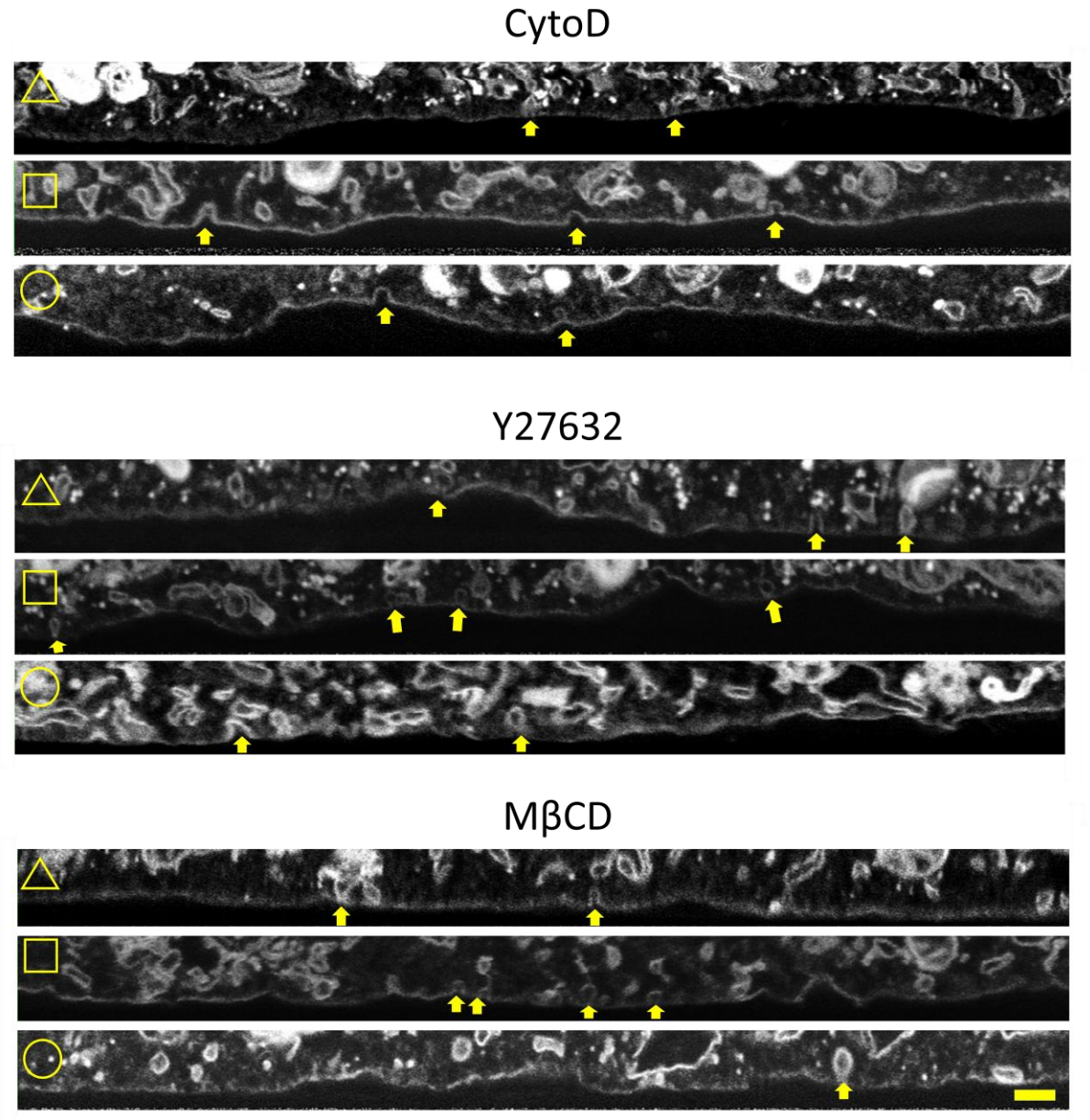

Supplementary Fig. 1 Representative high magnification micrographs focusing on the plasma membrane-substrate interface of circular, square and triangular hMSC micropatterns treated as indicated. Membrane invaginations in the range of 50-100 nm resembling caveolae are indicated by yellow arrows. Scale bar, 300 nm.

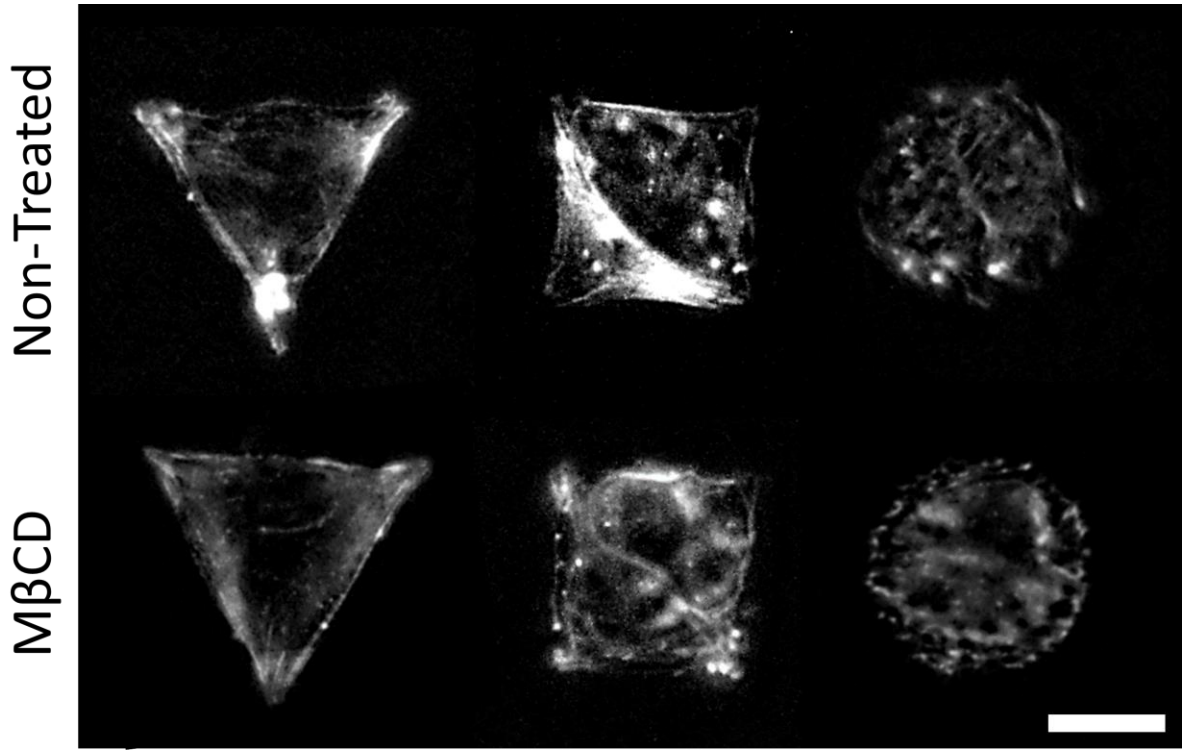

Supplementary Fig. 2 Representative fluorescence images of micropatterned hMSC treated with Methyl-β-Cyclodextrin (MβCD) for 24 hours followed by F-actin staining. Scale bar, 20 µm.

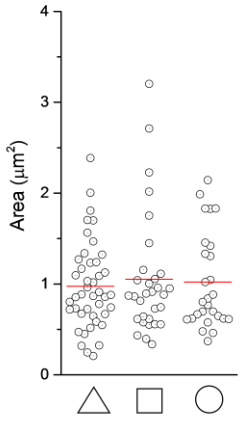

Supplementary Fig. 3 Quantification of the area between cell plasma membrane facing the substrate and the substrate in FIB cross sections of micropatterned triangular, square and circular hMSCs. Red line shows average.

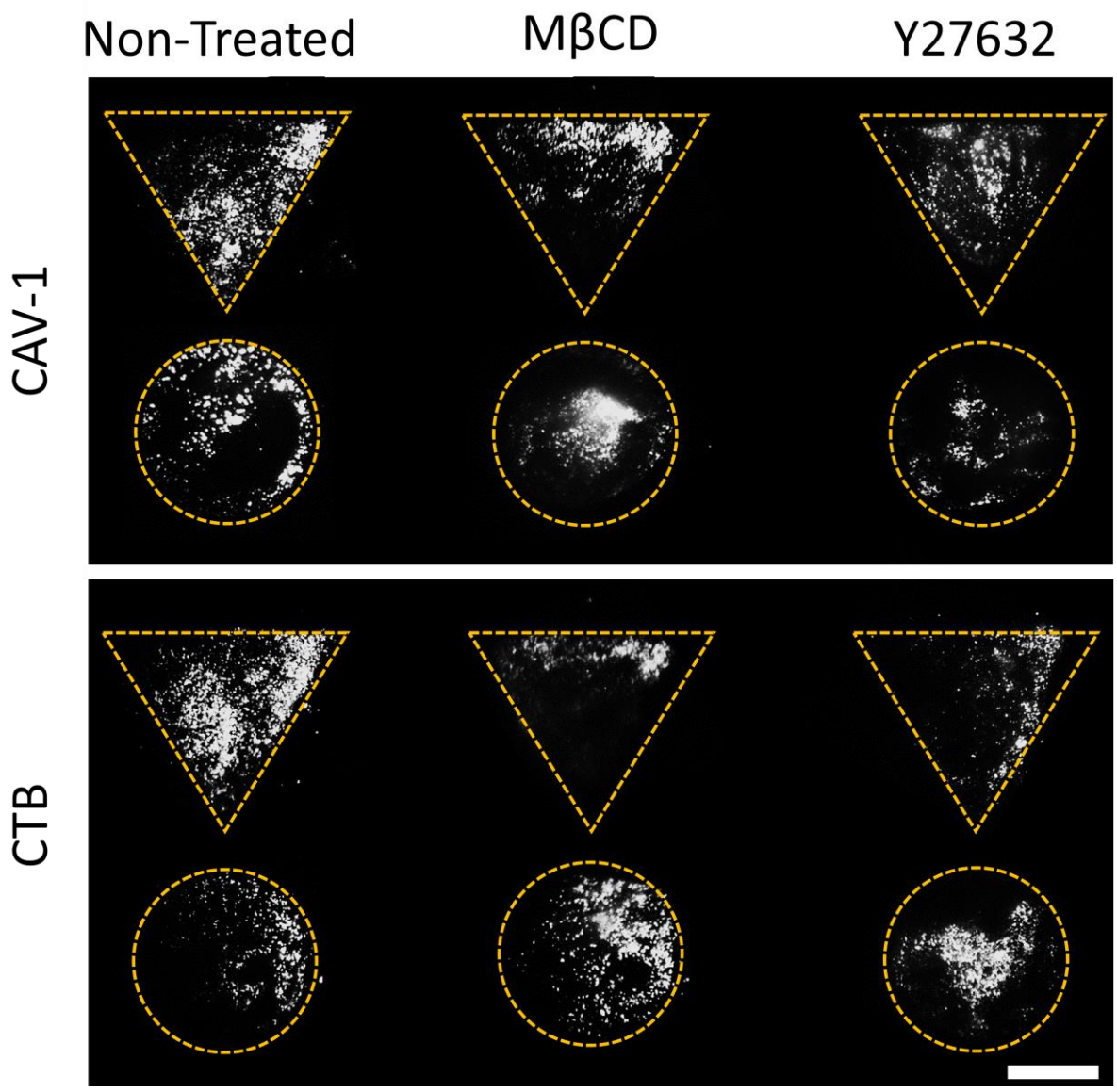

Supplementary Fig. 4 Representative TIRF images of micropatterned hMSC treated with either Methyl-β-Cyclodextrin (MβCD) or Y27632 for 24 hours followed by CTB or CAV-1 staining. Scale bar, 20 μm.

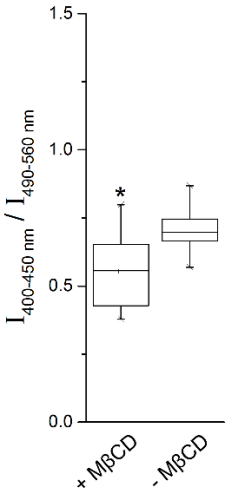

Supplementary Fig. 5 Quantification of the ratio of fluorescence intensity of the ordered ($I_{400-450\ nm}$) over disordered ($I_{490-560\ nm}$) phase emission of GPMVs isolated from hMSCs treated with or without methyl-beta-cyclodextrin (MβCD) (n = 10-20). Box plots show complete data range, bottom and top of box represent 25% and 75%, respectively. * equals $p<0.05$.

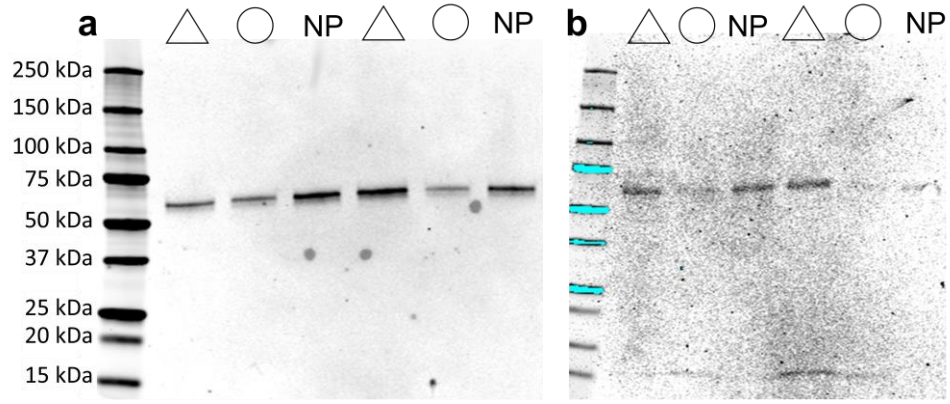

Supplementary Fig. 6 Non-cropped western blots of micropatterned and non-patterned (NP) hMSC. (a) Western blot using pan Akt antibody. (b) Western blot using Akt T308 antibody.

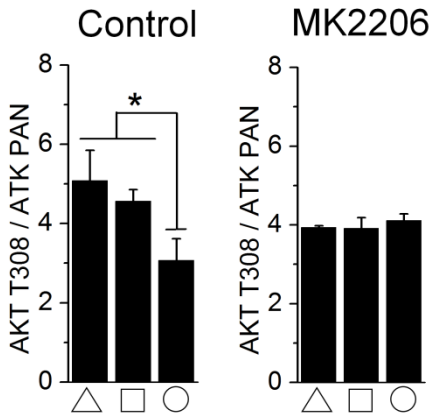

Supplementary Fig. 7 Quantification of data from ICWs of micropatterned hMSC stained for phospho-AKT T308 and pan AKT in the presence of an allosteric inhibitor of Akt (MK2206). Values are means ± S.D. * equals $p<0.05$ (3 independent experiments in duplicate).

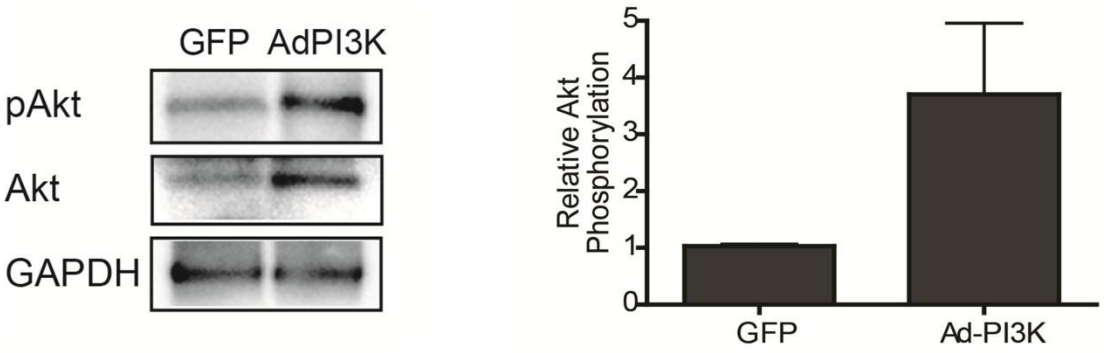

Supplementary Fig. 8 Western blot analysis of the phosphorylation level of Akt in hMSC overexpressing constitutively active PI3K compared to control GFP-expressing cells. Values are means ± S.D based on 3 independent experiments (n = 3).

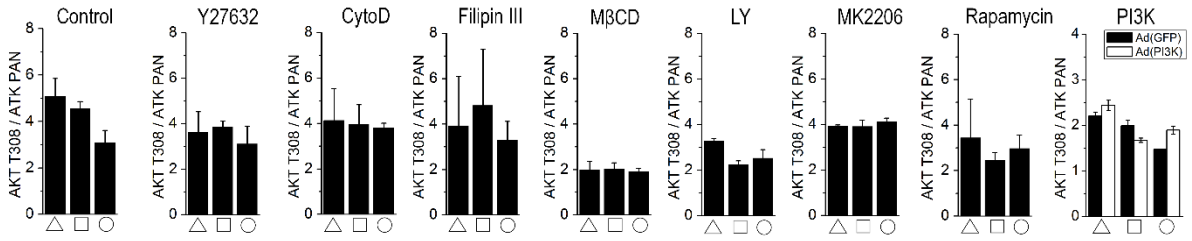

Supplementary Fig. 9 Quantification of data from ICWs of micropatterned hMSC stained for phospho-AKT T308 and pan AKT in the presence of inhibitors as indicated. Values are means ± S.D. * equals $p<0.05$ (1 experiment in duplicate).

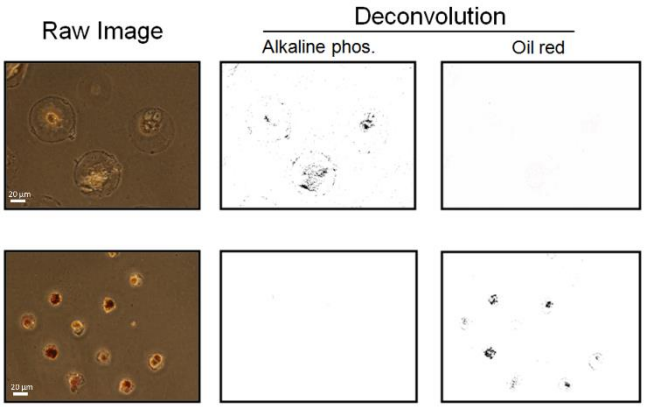

Supplementary Fig. 10 Example of color deconvolution based image quantification of hMSC differentiation. Representative images of hMSC on circular fibronectin islands of 3500 µm^2 (top) and 950 µm^2 (bottom) area stained with OilRedO and for alkaline phosphatase activity (left). Black and white images are binary images generated after color deconvolution (right). Note that micropatterns area used for data generation in all figures is an intermediate 1350 µm^2.